Miniature Gold Nanorods for Photoacoustic Molecular Imaging in the Second Near-Infrared Optical Window

Yun-Sheng Chen[1], **Yang Zhao**[2], **Soon Joon Yoon**[3], **Sanjiv Sam Gambhir**[1,2,4,*], and **Stanislav Emelianov**[5,6,*]

[1]Department of Radiology, School of Medicine, Canary Centre for Cancer Early Detection, Molecular Imaging Program at Stanford, Stanford University, Stanford, CA 94305

[2]Department of Materials Science and Engineering, Stanford University, Stanford, CA 94305

[3]Department of Bioengineering, University of Washington, Seattle, WA 98195

[4]Department of Bioengineering, Stanford University, Stanford, CA 94305

[5]School of Electrical and Computer Engineering, Georgia Institute of Technology, 777 Atlantic Drive, Atlanta, Georgia 30332, USA.

[6]Wallace H. Coulter Department of Biomedical Engineering, Georgia Institute of Technology and Emory University School of Medicine, 313 Ferst Drive, Atlanta, Georgia 30332, USA.

Abstract

In photoacoustic imaging, the second near infrared (NIR II) window is where tissue generates the least background signal. However, the large size of the few available contrast agents in this spectral range impedes their pharmacokinetics and decreases their thermal stability, leading to unreliable photoacoustic imaging. Here, we synthesize miniaturized gold nanorods absorbing in NIR II that are 5–11 times smaller than regular-sized gold nanorods with a similar aspect ratio. Under nanosecond pulsed laser illumination, small nanorods are about three times more thermally stable and generate 3.5 times stronger photoacoustic signal than absorption-matched large counterparts. These unexpected findings are confirmed using theoretical and numerical analysis,

showing that photoacoustic signal is not only proportional to the optical absorption of the nanoparticle solution but also to the surface-to-volume ratio of the nanoparticles. In living tumor bearing mice, these small targeted nanorods display a 30% improvement in efficiency of agent delivery to tumors and generate 4.5 times greater photoacoustic contrast.

Keywords

Photoacoustic imaging; contrast agents; molecular agents; gold nanorods

In biological tissue, there is relatively little optical absorption within two distinct spectral ranges: 650–900 nm and 1000–1200 nm, called the 1st (NIR I) and 2nd near-infrared (NIR II) windows respectively.[1] Within NIR II, 1050–1150 nm range is where blood-laden tissue generates the lowest photoacoustic background noise, produced from the optical absorption of deoxygenated hemoglobin.[2] Imaging in NIR II can significantly improve molecular photoacoustic imaging. However, one significant hurdle to date is the limited choices of contrast agents in this spectral range.

Common photoacoustic contrast agents include small chromophores, fluorescent proteins, and nanoparticles made from carbon, semiconductor, and plasmonic materials.[3, 4] Among these contrast agents, none of the fluorescent proteins can absorb in NIR II, and the small-molecule dyes, carbon nanotubes, and semiconductor nanoparticles in this window are largely uncharacterized for their cytotoxicity.[3–5] Plasmonic nanoparticles, such as gold nanorods (AuNRs), nanoplates, and nanoshells, have been widely used in NIR I for photoacoustic imaging and other biological and medical applications.[3, 6] Some of them also show strong optical absorption in NIR II. However, most of the plasmonic nanoparticles in NIR II have either high aspect ratios or large dimensions with extremely thin shells,[7] resulting in poor thermal stability, short blood circulation half-life, difficulty in extravasation, and low tissue penetration rate.

A seedless approach for miniature rods in near infrared II

AuNRs absorbing in NIR II usually have a relatively high aspect ratio of ~6, commonly grown with a seed-mediated approach (Figure 1a),[8–11] resulting in 80–150 nm (length) by 12–25 nm (width). To reduce the dimensions further, the size and number of gold seeds become the limiting factors. Alternatively, seedless approaches have shown to produce AuNRs with reduced sizes in NIR I,[12–14] and these relatively smaller AuNRs have shown improved pharmacokinetics and lower cytotoxicity compared to larger AuNRs.[15] However, the existing methods can only produce AuNRs with aspect ratios of up to five. As the aspect ratio increases, a complicated purification process is required to remove the increased amount of side products (nanospheres). By using hydroquinone as the reducing agent, one seedless method has recently produced high aspect ratio AuNRs, but with a relatively large size (13×87 nm).[16] For *in-vivo* applications, a critical size limit for nanoparticles is ~100 nm, beyond which the penetration of nanoparticles into tumors is limited.[17] The hydrodynamic length of the nanorods produced with the existing methods would approach or exceed 100 nm after conjugating molecular-specific ligands such as antibodies.

To reduce the size of AuNRs while maintaining the aspect ratio, several factors must be taken into account simultaneously. These factors include the concentration and type of the surfactant, the pH value of the growth solution, and the concentration of the reducing agent. $NaBH_{4(aq)}$ is a typical strong reducing agent that creates the nuclei by LaMer burst nucleation followed by fast random attachment and intraparticle ripening.[18] While using $NaBH_{4(aq)}$ at higher concentrations will create greater quantities of smaller AuNRs, the random nature of the nucleation process can result in a wide range of size distribution (Supplementary Fig. 1). Besides the number of nuclei, the pH value is a critical parameter in controlling the AuNR growth. The common ascorbic acid has a pK_a at 4.1. Decreasing the pH value below 4 significantly decreases its reduction potential, and thus slows down the growth rate, while on the other hand, improving the anisotropy.[11, 19] Compared to ascorbic acid, the reduction potential of hydroquinone also decreases with the pH value but at a higher rate (57 mV for each pH 1.0-value reduction), and therefore less acid is required to produce high aspect ratio rods. In fact, we observed that AuNRs stop growing when the pH value is lower than 2 in the hydroquinone growth solution. We intricately adjusted the concentration of $NaBH_{4(aq)}$ and the pH value of the growth medium, using the hydroquinone seedless method to reduce the size of long-aspect-ratio AuNRs while maintaining their mono-dispersity (Supplementary Information, Synthesis of Gold Nanorods). Our transmission electron microscopy (TEM) image (Figure 1d) shows that the smallest AuNRs obtained with this method are 8 ± 2 nm by 49 ± 8 nm.

As a reference for comparing the photoacoustic performance and thermal stability of AuNRs, we also synthesized regular-sized AuNRs (called large AuNRs from here on) with the seed-mediated method by using hydroquinone as the reducing agent.[10] TEM and SEM images show that the average size of these large AuNRs is approximately 18 ± 4 nm by 120 ± 17 nm (Figure 1e–f, Supplementary Fig. 2).

Improved photo-thermal stability

AuNRs can be photo-damaged under high intensity pulsed laser irradiation, causing optical absorption change and decay of photoacoustic signals.[20] Therefore, it is critical to measure the photo-damage threshold of AuNRs before comparing their photoacoustic performance. To test this threshold, we illuminated OD-matched AuNR solutions (Figure 1g) at various fluences with 200 pulses and recorded the relative photoacoustic response at each fluence (Supplementary Information, Photoacoustic Signal Characterization and Phantom Imaging).

At fluences below 6.1 mJ cm^{-2} (Figure 2a and Supplementary Fig. 3a), both small and large AuNRs show no obvious photoacoustic signal change; the signal fluctuation is mainly attributed to the intensity fluctuation of the laser system itself. At 8.7 mJ cm^{-2} (Supplementary Fig. 3b), small AuNRs show no measurable change in the photoacoustic signal, while the large AuNRs show an obvious 20% signal decline after the first 15 pulses and an overall 30% decline after 200 pulses. When we further increased the laser fluence to 18.2 mJ cm^{-2}, the large AuNR signal dropped by 42%, whereas the small AuNR signal decreased only by less than 10% after 200 pulses (Figure 2b). This result is particularly interesting because typically small anisotropic nanoparticles are considered less thermodynamically stable due to a large portion of surface atoms compared to their large

counterparts.[21, 22] Different from the prior studies, we found that small AuNRs are more photothermally stable than large AuNRs under nanosecond irradiation. Our SEM images (Figure 2 c–f) confirmed that most of the small AuNRs still maintain their shapes while more than 65% of the large AuNRs deform at 20 mJ cm^{-2}.

To test the limit of thermal stability, we illuminated both solutions with 1,000 pulses at 25 mJ cm^{-2}. In this extreme case, we observed that more than 50% of the small AuNRs still maintain their original shape, while the large AuNRs completely transform into spheres (Supplementary Fig. 4).

Pulsed laser irradiation photo-damages AuNRs through several possible mechanisms including vaporization, fragmentation, melting, and shape transition, depending on the laser intensity.[23, 24] As shown in the SEM images (Figure 2c–f), melting and shape transition could be the main mechanisms responsible for the photo-damage. Prior studies have shown that the melting temperature of gold nanoparticles decreases when their size reduces.[21, 22] Although melting can result in shape changes, the temperature at which AuNRs start undergoing morphological changes is not exactly at their melting temperature, but at a temperature called the shape-transition temperature.[25] The shape-transition temperatures are size-dependent and generally lower than the melting temperatures. For AuNRs containing less than 2,000 gold atoms, the shape-transition temperature is much lower than the melting temperature, but it increases at a faster rate than the melting temperature with respect to the increment of the AuNR volume. If a gold nanorod contains more than 8,000 gold atoms, both the melting and shape-transition temperatures gradually plateau. Theoretical calculations have shown that the shape-transition temperature of AuNRs ($>10^4$ gold atoms) approaches 1,000 K and its melting temperature is about 1,250 K.[25] The small and large AuNRs used in our experiments contain 1.4×10^5 and 1.6×10^6 atoms, respectively, which are well beyond the size where the shape-transition temperatures are highly size-dependent. Therefore, the difference in the shape-transition temperatures of both AuNRs should be negligible. One hypothesis of the enhanced thermal stability of the small AuNRs is their relatively lower peak temperature than the large AuNRs under the same laser illumination.

We numerically calculated the temperature profiles at the AuNR surface under the nanosecond laser heating (Figure 3b) (Supplementary Information, Numerical Simulations, and Supplementary Fig. 5). We used a laser fluence of 8.7 mJ cm^{-2} in the simulation, which will only damage the large AuNRs but not the small AuNRs as observed in our experiments. Additionally, we assumed that both small and large nanorods have the same interfacial thermal conductance of 150 MW m^{-2} K^{-1}, because these nanorods are within the size regime, in which with nanosecond laser illumination the small difference in their interfacial thermal conductance is negligible.[26] Our calculation shows that the peak temperature of the large AuNRs can reach almost 2,000 K which is significantly higher than the melting temperature of the large AuNRs. In contrast, the peak temperature of the small AuNRs reaches only ~800 K, which is lower than the shape-transition temperature, and likely an explanation for the insignificant photothermal damage observed. We also calculated the peak temperatures of the small AuNRs (8 nm in width) irradiated by higher laser fluences ranging from 10 to 25 mJ cm^{-2}. We found that the peak temperature increases linearly with the laser fluence at a slope of 60 K mJ^{-1} cm^2) (Supplementary Fig. 6); it requires 15 mJ cm^{-2} to heat

the 8-nm AuNR to 1,250 K, slightly lower than the laser damage threshold (20 mJ cm^{-2}) observed in our experiments. This discrepancy could be mainly attributed to two factors: (i) a plane-wave was used in our theoretical model, but the experiments were conducted using a laser beam with a Gaussian spatial distribution where Gaussian beam could introduce errors in estimating the actual laser fluence; and (ii) there was polydispersity of the AuNRs in the experiment, while in the simulations we assumed monodispersed nanoparticles.

Efficient photons-to-phonons converters

We first compared the photoacoustic signals from small and large AuNRs using a tube phantom (Figure 2g, left image). The 1st and the 3rd tubes (from left to right) contained small AuNR solutions, and the 2nd tube contained an OD-matched large AuNR solution. The 2nd and the 3rd tubes were relatively close to the centre of the transducer, and the 1st tube was near the edge of the transducer to exclude possible spatial variance of the laser fluence. In addition, large AuNRs scatter more light than small AuNRs while the photoacoustic intensity is dependent on optical absorption. To rule out the contribution to extinction caused by increased scattering from the large AuNRs, we compensated for the scattering effect with a higher OD of large AuNR solution in the 4th tube (1.5×OD at 1064 nm) to represent the worst-case scenario (Supplementary Information, Photoacoustic Signal Characterization and Phantom Imaging, and Supplementary Fig. 5). Figure 2h shows that the small AuNRs produced ~3.5 times higher photoacoustic signal than the OD-matched large AuNRs, and at least two times higher signal than the absorption-over-compensated large AuNRs (1.5×OD). The stronger photoacoustic signal from the small AuNRs seems contrary to the theory that photoacoustic intensity is only related to optical absorption when the Grüneisen parameter and laser fluence at the samples are the same.[27–29]

In conventional photoacoustic theory, the photoacoustic signal amplitude is the product of the Grüneisen coefficient, the absorption coefficient, and the local optical fluence.[29] However, this relationship is only true under the assumption that the laser pulse is short enough such that heat and stress cannot escape from the area of an optical absorber.[29] In a nanoparticle solution, light is mainly absorbed by the nanoparticles and not by solvent. Furthermore, due to the high thermal conductivity of gold and their nanometer volume, both heat and stress leak out of the nanoparticle during the irradiation of a nanosecond pulse.[30] Due to the time-dependent thermal leakage, the photoacoustic signal is determined by the heat transfer rate from gold to water.[31] In our photoacoustic experiments, the only difference between the AuNR solutions was the overall surface to volume ratio of the AuNRs in the solution, which increases as the size of the AuNRs decreases. We thus hypothesize that the photoacoustic enhancement originates from the increased surface-to-volume ratio of the small AuNRs, which promotes heat transfer.

To test our hypothesis, we theoretically studied the photoacoustic signal generation (Supplementary Information, Numerical Simulations). We first calculated the temperature profile of a AuNR (Figure 3b) and then used it to solve the time-dependent secondary differential photoacoustic wave equation to obtain the photoacoustic signal, which displays a familiar N-shape temporal profile (Figure 3c and Supplementary Fig. 7).

Photoacoustic generation is an energy conversion process similar to fluorescence where light is converted to light, and photovoltaics where light is converted to electricity. In photoacoustics, light is converted to ultrasound (or mechanical waves). The former energy conversion efficiencies are characterized using quantum yield and cell efficiency. Following this analogy, here we define a *photoacoustic quantum yield* (Φ_{PA}) to characterize the latter. The photoacoustic quantum yield is defined as the ratio of the emitted ultrasound energy ($E_{acoustic}$) to the absorbed photon energy (E_{optic}) from a single AuNR. Mathematically,

$$\Phi_{PA} = \frac{E_{acoustic}}{E_{optic}} = \frac{\iint p^2/R \, dSdt}{\int \sigma_a I dt} \quad (1)$$

where p is the generated photoacoustic signal, R is the acoustic impedance of water (mass density times velocity of sound), σ_a is the absorption cross-section of a single nanorod (Figure 3a), I is the input laser intensity, which is integrated over the time t of a single input laser pulse. The area S encloses a large spherical volume containing the nanorod, which is much larger than either the small or the large nanorod, ensuring that the generated heat does not escape from the volume during laser heating. Our calculation shows that the photoacoustic quantum yield, Φ_{PA}, follows a polynomial decay as the particle's volume increases (Figure 3d), and a small AuNR (8 nm in width) is ~200% more photoacoustically efficient than a large AuNR (18 nm in width).

While the photoacoustic quantum yield is conceptually easier to understand, it is more difficult to directly compare with the experimental data, because ultrasound transducers measure ultrasound amplitude, p, instead of energy in the experiments. During photoacoustic imaging, the peak amplitude of photoacoustic signals is measured for assessing photoacoustic performance. As we show in Supplementary Fig. 8 that the emitted acoustic energy is linearly proportional to the peak value of p^2, therefore, the measured photoacoustic signals during imaging can be related to the photoacoustic quantum yield, Φ_{PA}. Following the definition of photoacoustic quantum yield, it becomes obvious that to compare the peak amplitude of p between two AuNR samples, their optical absorption needs to be matched. The photoacoustic signal from each nanorod sample (solutions or a single nanorod) with the matched optical absorption is denoted as P, where P can be deduced from the photoacoustic quantum yield,

$$P \propto \sqrt{\phi_{PA}/\sigma_a} \quad (2)$$

Figure 3e confirms that the emitted acoustic energy from each AuNR is linearly proportional to its surface area, which leads to a linear relationship between the photoacoustic quantum yield and the surface-to-volume ratio of each nanorod (Figure 3f). As a result of the quadratic relation between amplitude and energy, when the optical absorption is matched across AuNR samples with different nanorod sizes, photoacoustic signal amplitude is quadratically proportional to the surface-to-volume ratio of the AuNR (Figure 3f). Our numerical calculation indicates that when the optical absorption of the AuNR solutions is

matched, small AuNRs (8 nm in width) can generate more than 3.5 times higher photoacoustic signal than the large AuNRs (18 nm in width), matching well with what we observed in the *in-vitro* experiments.

Efficient agent-delivery to tumors with molecular targeting

To characterize the targeting specificity of the small AuNRs, we functionalized both large and small AuNRs with GRPR-targeting peptides and Cy5 dyes (Figure 1c),[32] and confirmed each surface functionalization step by measuring the zeta potentials (Figure 4a).[33] GRPR is one of the G-coupled protein receptors that control cell functions including proliferation, motility, etc. GRPR has been found to be overexpressed in many cancers including breast, colon, lung, and prostate cancers, and is thus of great interest for *in-vivo* molecular photoacoustic imaging.[34]

We tested the targeting specificity with PC-3 (GRPR+) and DU-145 (GRPR-) cell lines using fluorescent imaging of Cy5 dye (Figure 4b–j).[35] The results demonstrate the targeting specificity of our GRPR-targeting AuNRs.

To validate our small AuNRs as photoacoustic molecular imaging agents, we performed *in vivo* photoacoustic imaging using a murine model of prostate cancer. Five groups of mice were used in our study with each group containing three six-weeks-old male nu/nu mice. We allowed the subcutaneous tumors to grow to ~1 cm in diameter. In groups 1 to 4, we tail-vein injected one of the four types of AuNR solutions with matched OD. The four solutions were large non-targeted (PEG) AuNRs (group 1), small non-targeted (PEG) AuNRs (group 2), large GRPR-targeted AuNRs (group 3), and small GRPR-targeted AuNRs (group 4). Twenty-four hours after injection, we randomly chose one mouse from each group for photoacoustic imaging and labelled the mice from group 1 to group 4 as m1 to m4, respectively. We used a pulsed laser irradiation at 1064 nm with a fluence of 25 mJ cm^{-2} and scanned each animal from tail to head (Figure 5a). The laser fluence used here was slightly higher than the damage threshold of the small AuNRs to compensate for the decay and diffusion of light inside the skin. With the non-targeted AuNRs, we observed slightly higher signal from the large AuNRs (Figure 5a) than that from the small AuNRs (Figure 5b), which could be attributed to tumor heterogeneity although our statistical analysis shows that the difference is insignificant (Figure 5g). Distinctively, in the case of the GRPR-targeted AuNRs, the small AuNRs (Figure 5d) show statistically significant higher photoacoustic signal than the OD-matched large AuNRs (Figure 5c), confirming small AuNRs have enhanced photoacoustic-signal-generation efficiency, higher tumor-penetration efficiency, and higher binding specificity compared to their large counterparts. Interestingly, we also observed a decay of the photoacoustic signal from the targeted large AuNRs close to the end of the scan (Figure 5c), which is possibly due to the thermal instability of the large AuNRs, as observed in the *in-vitro* study (Figure 2). Due to the enhanced thermal stability, there was no signal decay seen in the targeted small AuNRs (Figure 5d) over the entire scan. We used the fifth group of mice for blocking test that further confirmed the GRPR-targeting specificity of our targeted AuNRs (Supplementary Fig. 10).

Another 24 hours after the *in-vivo* imaging, we sacrificed all the mice in groups 1 to 4 and collected their main organs and tumors for more quantitative analysis. Fluorescent imaging of the major organs (Figure 5e, showing m4 as an example) indicates that nanoparticles were mainly accumulated in the tumor and the liver. Fluorescent imaging of the tumors shows the highest signal from group 4 (Figure 5f, g) and confirms the favorable pharmacokinetics and highest targeting specificity of the targeted small AuNRs, which manifest almost twice amount of signal than the targeted large AuNRs and non-targeted AuNRs.

Conclusions

A stable photoacoustic signal is critical for achieving quantitative photoacoustic imaging, because one of the most important assumptions is the constant optical absorption of the molecular imaging agent. An unstable photoacoustic signal will result in ambiguous evaluation of molecular imaging agent concentrations, potentially misleading the diagnosis and leading to suboptimal therapy. In this study, we have developed a protocol to synthesize the smallest AuNRs absorbing at 1064 nm, a wavelength within the NIR II window, which ensures low background noise from endogenous absorbers in tissue. We found that our small AuNRs are 3 times more thermally stable than the large AuNRs under nanosecond laser irradiation. More importantly, we have also discovered that by simply reducing the size without altering the optical absorption of nanoparticles, we can significantly increase the photoacoustic quantum yield of nanoparticles by ~200% which leads to high photoacoustic signal enhancement by more than 3.5 fold. *In vivo*, these targeted miniature AuNRs display significant improvement in overall tumor photoacoustic signal as compared to their large counterparts due to enhanced delivery, targeting, thermal stability, and their surface-to-volume ratio. These findings provide an additional strategy for the design of future photoacoustic molecular contrast agents and will possibly motivate more photoacoustic molecular imaging applications in the second NIR window.

Supplementary Material

Refer to Web version on PubMed Central for supplementary material.

ACKNOWLEDGEMENTS

REFERENCES

1. Smith AM, Mancini MC & Nie S Bioimaging: Second window for in vivo imaging. Nature Nanotechnology 4, 710–711 (2009).

2. Homan K et al. Prospects of molecular photoacoustic imaging at 1064 nm wavelength. Optics Letters 35, 2663–2665 (2010). [PubMed: 20680092]

3. Weber J, Beard PC & Bohndiek SE Contrast agents for molecular photoacoustic imaging. Nature Methods 13, 639–650 (2016). [PubMed: 27467727]

4. Nie LM & Chen XY Structural and functional photoacoustic molecular tomography aided by emerging contrast agents. Chemical Society Reviews 43, 7132–7170 (2014). [PubMed: 24967718]

5. Jiang Y et al. Broadband absorbing semiconducting polymer nanoparticles for photoacoustic imaging in second near-infrared window. Nano Letters 17, 4964–4969 (2017). [PubMed: 28654292]

6. Ashraf S et al. in Light-responsive nanostructured systems for applications in nanomedicine. (ed. Sortino S) 169–202 (Springer International Publishing, Cham; 2016).

7. Li WW & Chen XY Gold nanoparticles for photoacoustic imaging. Nanomedicine 10, 299–320 (2015). [PubMed: 25600972]

8. Jana NR, Gearheart L & Murphy CJ Seed-mediated growth approach for shape-controlled synthesis of spheroidal and rod-like gold nanoparticles using a surfactant template. Advanced Materials 13, 1389–1393 (2001).

9. Nikoobakht B & El-Sayed MA Preparation and growth mechanism of gold nanorods (nrs) using seed-mediated growth method. Chemistry of Materials 15, 1957–1962 (2003).

10. Vigderman L & Zubarev ER High-yield synthesis of gold nanorods with longitudinal SPR peak greater than 1200 nm using hydroquinone as a reducing agent. Chemistry of Materials 25, 1450–1457 (2013).

11. Wu H-Y, Chu H-C, Kuo T-J, Kuo C-L & Huang MH Seed-mediated synthesis of high aspect ratio gold nanorods with nitric acid. Chemistry of Materials 17, 6447–6451 (2005).

12. Ali MRK, Snyder B & El-Sayed MA Synthesis and optical properties of small au nanorods using a seedless growth technique. Langmuir 28, 9807–9815 (2012). [PubMed: 22620850]

13. Song J et al. Ultrasmall gold nanorod vesicles with enhanced tumor accumulation and fast excretion from the body for cancer therapy. Advanced Materials 27, 4910–4917 (2015). [PubMed: 26198622]

14. Jia H et al. Synthesis of absorption-dominant small gold nanorods and their plasmonic properties. Langmuir 31, 7418–7426 (2015). [PubMed: 26079391]

15. Li Z et al. Metabolizable small gold nanorods: size-dependent cytotoxicity, cell uptake and in vivo biodistribution. ACS Biomaterials Science & Engineering 2, 789–797 (2016).

16. Xu X et al. Seedless synthesis of high aspect ratio gold nanorods with high yield. Journal of Materials Chemistry A 2, 3528–3535 (2014).

17. Perrault SD, Walkey C, Jennings T, Fischer HC & Chan WCW Mediating tumor targeting efficiency of nanoparticles through design. Nano Letters 9, 1909–1915 (2009). [PubMed: 19344179]

18. Thanh NT, Maclean N & Mahiddine S Mechanisms of nucleation and growth of nanoparticles in solution. Chemical reviews 114, 7610–7630 (2014). [PubMed: 25003956]

19. Bullen C, Zijlstra P, Bakker E, Gu M & Raston C Chemical kinetics of gold nanorod growth in aqueous CTAB solutions. Crystal Growth & Design 11, 3375–3380 (2011).

20. Chen Y-S et al. Enhanced thermal stability of silica-coated gold nanorods for photoacoustic imaging and image-guided therapy. Optics Express 18, 8867–8878 (2010). [PubMed: 20588732]

21. Qi WH & Wang MP Size and shape dependent melting temperature of metallic nanoparticles. Materials Chemistry and Physics 88, 280–284 (2004).

22. Zhu J, Fu Q, Xue Y & Cui Z Accurate thermodynamic relations of the melting temperature of nanocrystals with different shapes and pure theoretical calculation. Materials Chemistry and Physics 192, 22–28 (2017).

23. González-Rubio G, Guerrero-Martínez A & Liz-Marzán LM Reshaping, fragmentation, and assembly of gold nanoparticles assisted by pulse lasers. Accounts of Chemical Research 49, 678–686 (2016). [PubMed: 27035211]

24. González-Rubio G et al. Femtosecond laser reshaping yields gold nanorods with ultranarrow surface plasmon resonances. Science 358, 640–644 (2017). [PubMed: 29097547]

25. Wang Y & Dellago C Structural and morphological transitions in gold nanorods: a computer simulation study. The Journal of Physical Chemistry B 107, 9214–9219 (2003).

26. Metwally K, Mensah S & Baffou G Fluence threshold for photothermal bubble generation using plasmonic nanoparticles. The Journal of Physical Chemistry C 119, 28586–28596 (2015).

27. Oraevsky AA, Jacques SL, Esenaliev RO & Tittel FK Laser-based optoacoustic imaging in biological tissues. Proc. SPIE 2134, Laser-Tissue Interaction V; and Ultraviolet Radiation Hazards 2134, 122–128 (1994).

28. Cox BT & Beard PC Fast calculation of pulsed photoacoustic fields in fluids using k-space methods. The Journal of the Acoustical Society of America 117, 3616–3627 (2005). [PubMed: 16018465]

29. Xu M & Wang LV Photoacoustic imaging in biomedicine. Review of scientific instruments 77, 041101 (2006).

30. Nguyen SC et al. Study of heat transfer dynamics from gold nanorods to the environment via time-resolved infrared spectroscopy. ACS Nano 10, 2144–2151 (2016). [PubMed: 26840805]

31. Chen Y-S, Frey W, Aglyamov S & Emelianov S Environment-dependent generation of photoacoustic waves from plasmonic nanoparticles. Small 8, 47–52 (2012). [PubMed: 22114029]

32. Cornelio DB, Roesler R & Schwartsmann G Gastrin-releasing peptide receptor as a molecular target in experimental anticancer therapy. Annals of Oncology 18, 1457–1466 (2007). [PubMed: 17351255]

33. Levi J, Sathirachinda A & Gambhir SS A high-affinity, high-stability photoacoustic agent for imaging gastrin-releasing peptide receptor in prostate cancer. Clinical Cancer Research 20, 3721–3729 (2014). [PubMed: 24850845]

34. Ischia J, Patel O, Bolton D, Shulkes A & Baldwin GS Expression and function of gastrin-releasing peptide (GRP) in normal and cancerous urological tissues. BJU International 113, 40–47 (2014). [PubMed: 24894852]

35. Maddalena ME et al. 177Lu-AMBA biodistribution, radiotherapeutic efficacy, imaging, and autoradiography in prostate cancer models with low GRP-R expression. Journal of Nuclear Medicine 50, 2017–2024 (2009). [PubMed: 19910427]
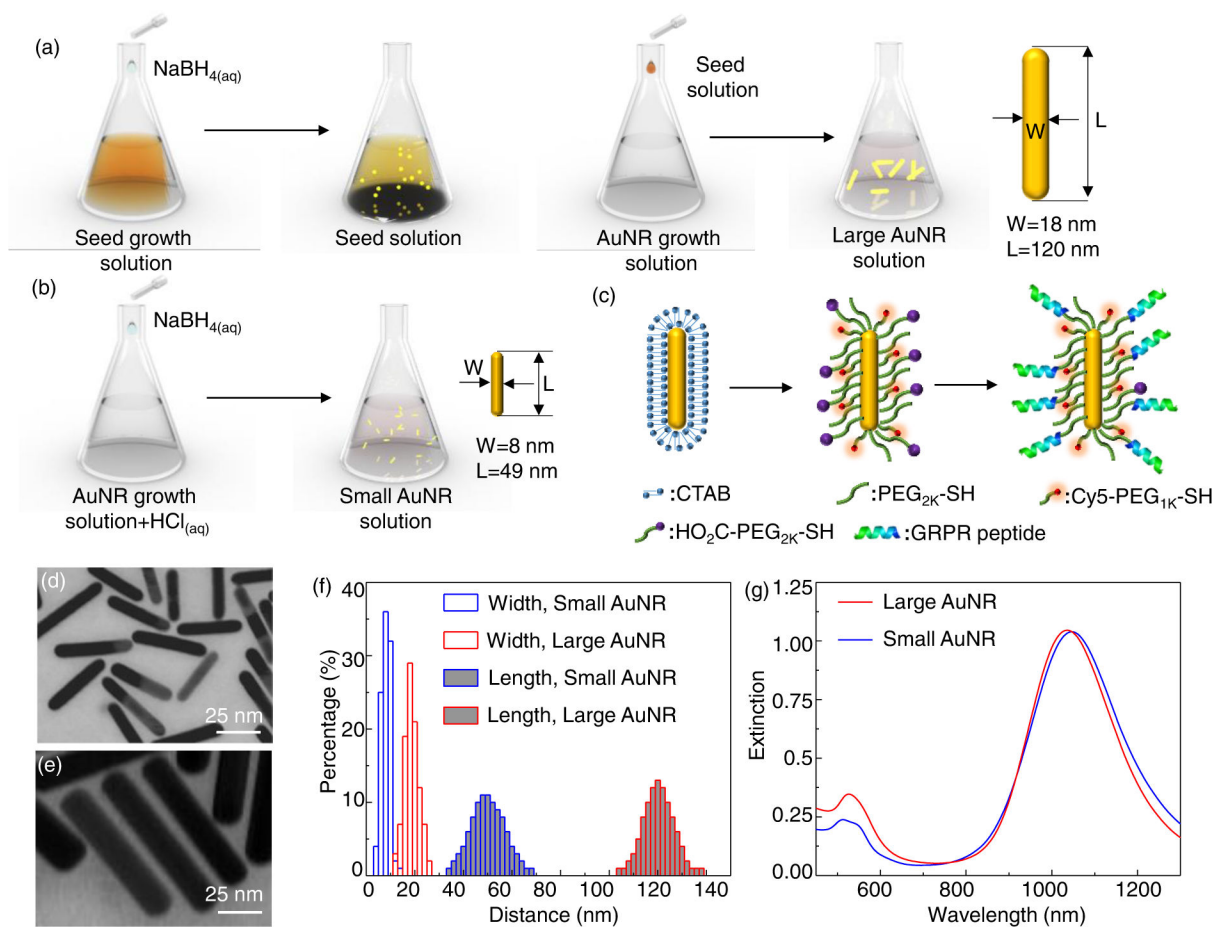
Figure 1. Synthesis procedure of small and large AuNRs and size characterization.
(a) Illustration of seed-mediated growth to produce large AuNRs with dimensions of 18 nm by 120 nm. (b) Illustration of seedless growth to produce small AuNRs with dimensions of 8 nm by 49 nm. (c) Illustration of surface functionalization of the AuNRs for targeting GRPR on prostate cancer cells. Transmission electron microscope (TEM) images of as synthesized (d) small and (e) large AuNRs. (f) Size distribution of the AuNRs, confirming the small AuNRs with dimensions of 8 nm by 49 nm and the large AuNRs with dimensions of 18 nm by 120 nm. (g) Normalized extinction spectra of the large and small AuNRs, measured with UV-vis spectroscopy. The increased extinction at shorter wavelengths from large AuNRs indicates their relatively larger scattering cross-section.
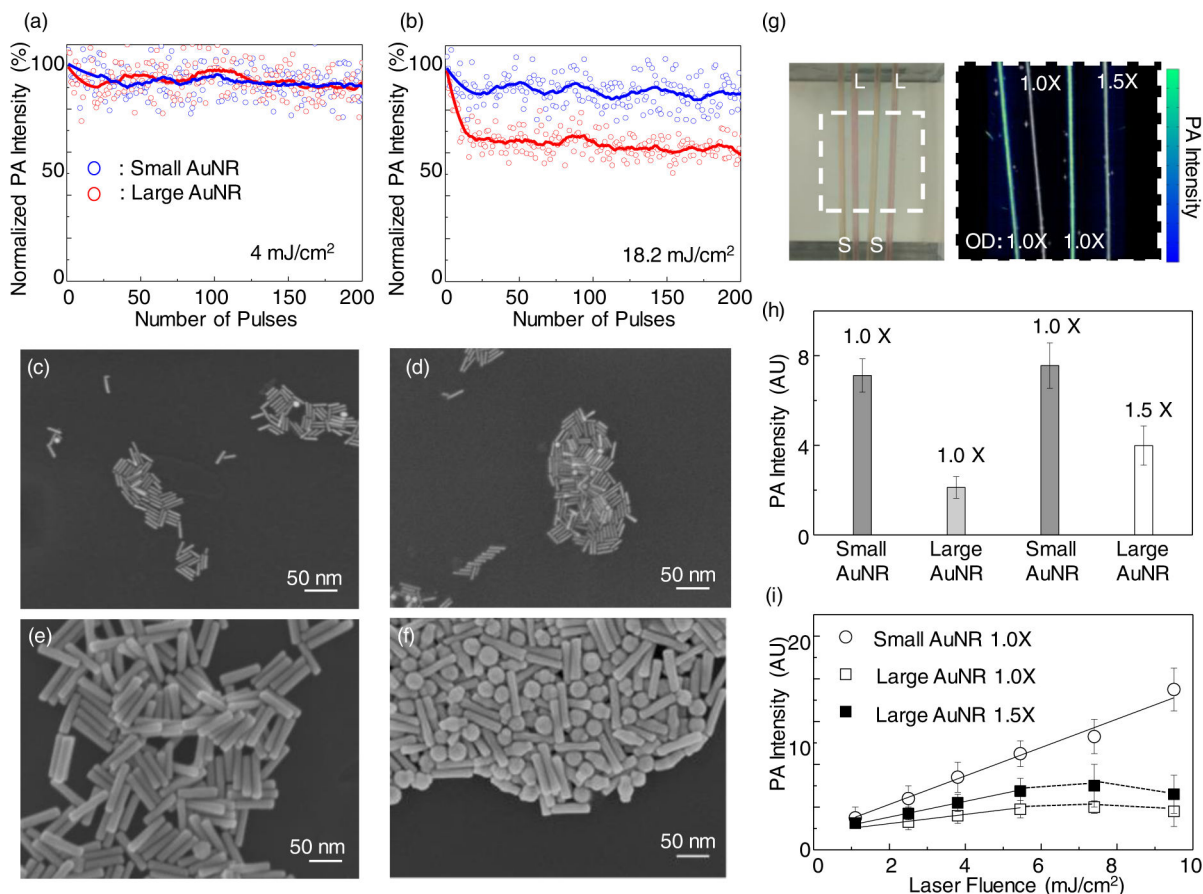
Figure 2. Comparison of thermal stability of small and large AuNRs.

OD-matched small (blue) and large (red) AuNRs illuminated with 200 laser pulses at (a) 4.0 mJ cm^{-2}, and (b) 18.2 mJ cm^{-2}. The solid lines are moving average of the data points. SEM images of small AuNRs (c) before and (d) after 200 laser pulses at 20 mJ cm^{-2}, showing that majority small AuNRs maintain their rod shape. SEM images of large AuNRs (e) before and (f) after 200 laser pulses at 20 mJ cm^{-2}, showing that ~65% of the large AuNRs are thermally destroyed. (g) A photograph of a tube phantom containing AuNR solutions, from left to right (1st to 4th tubes): small AuNRs (OD = 3), large AuNRs (OD =3), small AuNRs (OD = 3), and large AuNRs (OD = 4.5). The field of view of the photoacoustic image is 13.9 mm × 13.3 mm. (h) Photoacoustic intensities from the tube phantoms, show comparable signals from the first and third tubes containing identical small AuNRs, which are ~3.5 times higher than the second tube containing OD-matched large AuNRs and ~1.9 times higher than the fourth tube containing OD-over-compensated large AuNRs. The centre values are the mean values of the photoacoustic intensities (n= 290) of each tube phantom, and the error bars are the standard deviation. (i) Photoacoustic intensities as a function of laser fluences. The linear dependence of small AuNRs indicates their enhanced thermal stability, compared with the decreased photoacoustic intensities of large AuNRs at higher laser fluences. The centre values are the mean values (n=200), and the error bars are the standard deviation. We repeated each test independently for 3 times and received similar results.
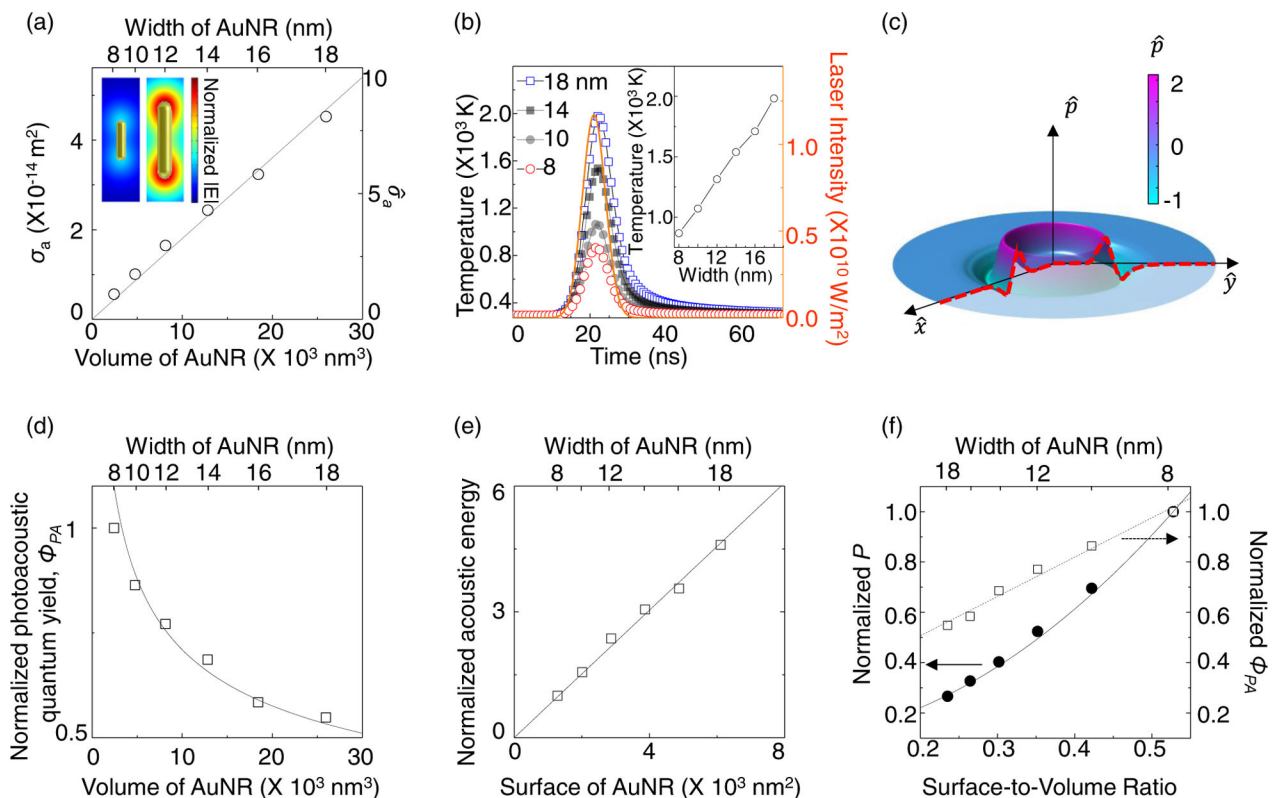
Figure 3. Numerical analysis of photoacoustic signal generation from small and large AuNRs.
Only one nanorod is considered in each simulation domain. (a) FDTD simulations of absorption cross-section (σ_a) of AuNRs with various sizes. The solid curve is linear regression. The left (right) y-axis shows the absolute (normalized) values of the absorption cross-section. When the incident light is linearly polarized along the long axis, electric fields are concentrated at the two ends of the rods (insets). (b) Simulated transient temperature profile on the AuNR surface using COMSOL. The incident laser pulse has a Gaussian temporal profile, shown as the solid red curve (right y-axis), with an input fluence of 8.7 mJ cm^{-2} at 1064 nm. Peak temperatures of AuNRs are summarized in the inset. (c) Spatial distribution of the normalized photoacoustic signal of the 18-nm AuNRs, showing the signature N-shape. (d) Normalized photoacoustic quantum yield, ϕ_{PA} as a function of the nanoparticle volumes, showing that smaller AuNR exhibits a higher photoacoustic quantum yield. (e) Normalized emitted acoustic energy as a function of nanoparticle surface areas, showing a linear relationship. (f) Normalized peak amplitude of the photoacoustic signal, P, and photoacoustic quantum yield, ϕ_{PA}, as a function of the surface-to-volume ratio of the AuNRs, showing that ϕ_{PA} is linearly proportional to the surface-to-volume ratio, and P is approximately quadratic to the surface-to-volume ratio. The solid curve is quadratic fitting, and the dashed line is linear fitting. All normalizations are with respect to the 8-nm AuNR. Symbols and description are detailed in Supplementary Table 2.
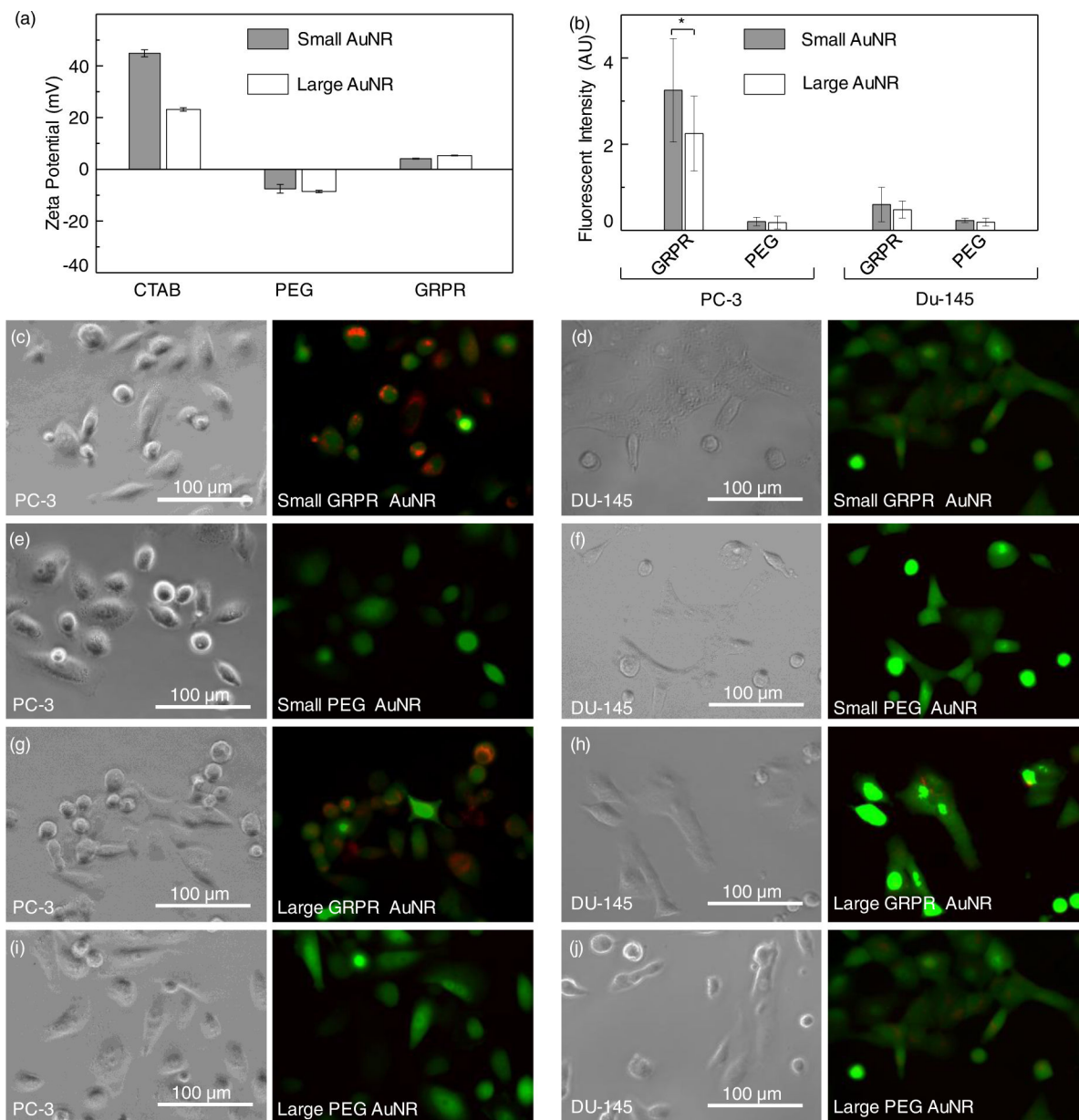
Figure 4. Targeting specificity of small and large AuNRs for prostate cancer cells.
All cells were genetically encoded with green fluorescent proteins for imaging. (a) Zeta potential measurements of the AuNRs at each surface functionalization step. The centre values are the mean values (n=36), and error bars are the standard deviation. (b) Fluorescent intensities of Cy5 from 30 cancer cells incubated either with targeted (GRPR) or non-targeted (PEG) AuNRs. Higher intensities reflect higher targeting efficiency. The centre values are the mean values (n=30), and error bars are the standard deviation. * p=0.000472 (two-tailed p-value). Bright field and fluorescent images of (c) small targeted AuNRs on PC-3 (GRPR+) cells, strong Cy5 signals indicate efficient targeting; (d) small targeted AuNRs on DU-145 (GRPR-) cells, relatively weak Cy5 signals indicate low targeting efficiency because of the low density of GRPR on this cell line; (e) small non-targeted (PEG terminated) AuNRs on PC-3 cells, weak Cy5 signals indicate good targeting specificity; (f)

small non-targeted AuNRs on DU-145 cells, minimal Cy5 signals indicate minimal nonspecific binding; (g) large targeted AuNRs on PC-3 cells, strong Cy5 signals indicate efficient targeting; (h) large targeted AuNRs on DU-145 cells, weak Cy5 signals indicate good targeting specificity; (i) large non-targeted AuNRs on PC-3 cells, weak Cy5 signals indicate good targeting specificity; and (j) large non-targeted AuNRs on DU-145 cells, minimal Cy5 signals indicate minimal nonspecific binding. Field-of-view of (c)-(j) is 275 μm × 200 μm. We repeated the imaging experiments independently for 3 times and received similar results.
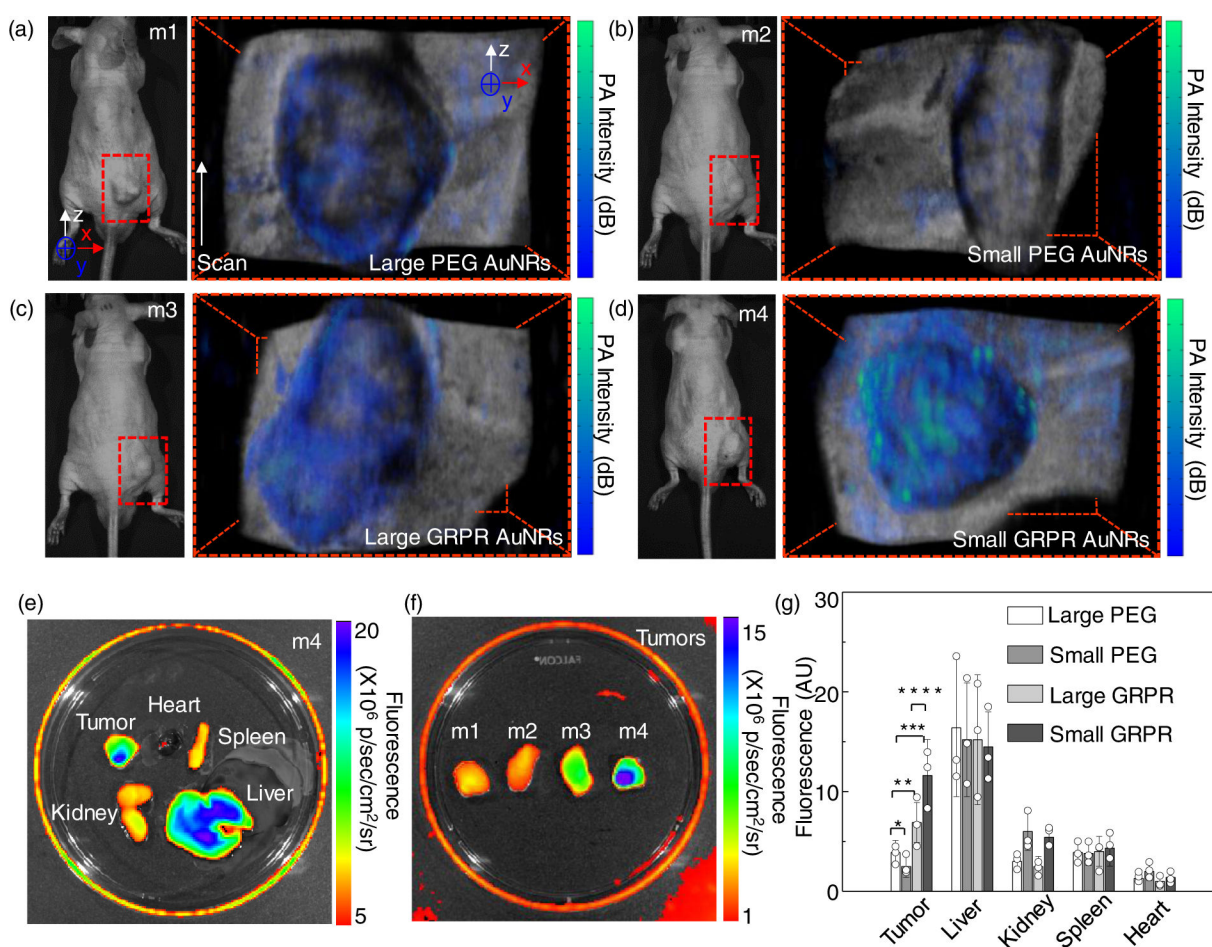
Figure 5. Imaging of targeted small and large AuNRs in a murine model of prostate cancer.
Photograph and photoacoustic imaging of tumor-bearing mouse with non-targeted (a) large
and (b) small AuNRs; and with targeted (c) large and (d) small AuNRs. The photoacoustic
signal intensities are displayed as colour maps, overlaid with the ultrasound images for
anatomical information. The in vivo photoacoustic imaging is done with one replicate. The
scanning volume for panels (a) to (d) is 23 mm (x) × 19 mm (y) × 16 mm (z). (e) A
representative fluorescent image of harvested kidney, tumor, heart, spleen and liver from the
tumor-bearing mouse with targeted small AuNRs, showing that these nanoparticles are most
aggregated at the tumor and the liver. Similar results are received from all three mice in the
same group. (f) Represent fluorescent imaging of the harvested tumors from 4 mice, m1 to
m4, showing strongest signal from the mouse in group 4, which is GRPR-targeted small
AuNRs, demonstrating their highest binding specificity and efficiency. Similar results are
received from all three mice in each group. (g) Collective measurements of the fluorescent
intensities from the major organs and tumors from the 4 groups of mice, indicating that all
AuNRs will accumulate mainly at the liver and similarly at the other organs, but only small
GRPR-targeted AuNRs show highest binding specificity at the tumor site. The centre values
are the mean values (n=3), and error bars are the standard deviation,* p=0.3915, **
p=0.0484, *** p=0.0053, ****p=0.0398 (two-tailed p-value).